A&A 664, A130 (2022)
https://doi.org/10.1051/0004-6361/202141546

Astronomy & Astrophysics

Physical properties of the trans-Neptunian object (38628) Huya from a multi-chord stellar occultation

P. Santos-Sanz[1], J. L. Ortiz[1], B. Sicardy[2], M. Popescu[3,4], G. Benedetti-Rossi[2,5,6], N. Morales[1], M. Vara-Lubiano[1], J. I. B. Camargo[7,5], C. L. Pereira[7,5], F. L. Rommel[7,5], M. Assafin[8,5], J. Desmars[9,10], F. Braga-Ribas[11,2,5,7], R. Duffard[1], J. Marques Oliveira[2], R. Vieira-Martins[5,7], E. Fernández-Valenzuela[12], B. E. Morgado[2,5,7], M. Acar[13,14], S. Anghel[3,10,15], E. Atalay[16], A. Ateş[13], H. Bakış[17], V. Bakıs[17], Z. Eker[17], O. Erece[17,18], S. Kaspi[19], C. Kayhan[13,20], S. E. Kilic[18], Y. Kilic[17,18], I. Manulis[21], D. A. Nedelcu[3], M. S. Niaei[16], G. Nir[21], E. Ofek[21], T. Ozisik[18], E. Petrescu[22], O. Satir[16], A. Solmaz[23,24], A. Sonka[3], M. Tekes[23], O. Unsalan[25], C. Yesilyaprak[16,26], R. Anghel[27], D. Berteşteanu[28], L. Curelaru[29], C. Danescu[30], V. Dumitrescu[31], R. Gherase[28,32], L. Hudin[33], A-M. Stoian[34], J. O. Tercu[34,35], R. Truta[36], V. Turcu[37], C. Vantdevara[38], I. Belskaya[39], T. O. Dementiev[40], K. Gazeas[41], S. Karampotsiou[41], V. Kashuba[42], Cs. Kiss[43,44], N. Koshkin[42], O. M. Kozhukhov[40], Y. Krugly[39], J. Lecacheux[2], A. Pal[43], Ç. Püsküllü[45,46], R. Szakats[43], V. Zhukov[42], D. Bamberger[47], B. Mondon[48], C. Perelló[49,50], A. Pratt[51,50], C. Schnabel[49,50], A. Selva[49,50], J. P. Teng[52], K. Tigani[53], V. Tsamis[53], C. Weber[50], G. Wells[47], S. Kalkan[54], V. Kudak[55], A. Marciniak[56], W. Ogłoza[57], T. Özdemir[58], E. Pakštienė[59], V. Perig[55], and M. Żejmo[60]

(Affiliations can be found after the references)

Received 14 June 2021 / Accepted 30 April 2022

ABSTRACT

Context. As part of our international program aimed at obtaining accurate physical properties of trans-Neptunian objects (TNOs), we predicted a stellar occultation by the TNO (38628) Huya of the star *Gaia* DR2 4352760586390566400 (m_G = 11.5 mag) on March 18, 2019. After an extensive observational campaign geared at obtaining the astrometric data, we updated the prediction and found it favorable to central Europe. Therefore, we mobilized half a hundred of professional and amateur astronomers in this region and the occultation was finally detected by 21 telescopes located at 18 sites in Europe and Asia. This places the Huya event among the best ever observed stellar occultation by a TNO in terms of the number of chords.

Aims. The aim of our work is to determine an accurate size, shape, and geometric albedo for the TNO (38628) Huya by using the observations obtained from a multi-chord stellar occultation. We also aim to provide constraints on the density and other internal properties of this TNO.

Methods. The 21 positive detections of the occultation by Huya allowed us to obtain well-separated chords which permitted us to fit an ellipse for the limb of the body at the moment of the occultation (i.e., the instantaneous limb) with kilometric accuracy.

Results. The projected semi-major and minor axes of the best ellipse fit obtained using the occultation data are (a', b') = (217.6 ± 3.5 km, 194.1 ± 6.1 km) with a position angle for the minor axis of P' = 55.2° ± 9.1. From this fit, the projected area-equivalent diameter is 411.0 ± 7.3 km. This diameter is compatible with the equivalent diameter for Huya obtained from radiometric techniques (D = 406 ± 16 km). From this instantaneous limb, we obtained the geometric albedo for Huya (p_V = 0.079 ± 0.004) and we explored possible three-dimensional shapes and constraints to the mass density for this TNO. We did not detect the satellite of Huya through this occultation, but the presence of rings or debris around Huya was constrained using the occultation data. We also derived an upper limit for a putative Pluto-like global atmosphere of about p_{surf} = 10 nbar.

Key words. Kuiper belt objects: individual: Huya – methods: observational – techniques: photometric

1. Introduction

The stellar occultation technique is a very direct way to obtain highly accurate sizes and to derive albedos, as well as, in some cases, even the densities and 3D shapes for trans-Neptunian objects (TNOs, e.g., Sicardy et al. 2011; Ortiz et al. 2012, 2017). Atmospheres and satellites can also be detected and characterized via stellar occultations (Sicardy et al. 2006; Meza et al. 2019). Minute details that are otherwise undetectable by any other ground-based technique may also be detected using stellar occultations, such as the rings detected around the centaurs Chariklo (Braga-Ribas et al. 2014) and Chiron (Ortiz et al. 2015; Ruprecht et al. 2015) and around the dwarf planet Haumea (Ortiz et al. 2017). These discoveries have opened a new way of research within the planetary sciences of the distant solar system bodies (Sicardy et al. 2019, 2020). All of the above demonstrates how the stellar occultation technique serves as a powerful means of obtaining information on the physical properties of TNOs.

From October 2009 onwards, when the first stellar occultation by a TNO (apart from Pluto) was recorded (Elliot et al. 2010), to date, about 77 stellar occultations produced by 33 different TNOs, excluding the one presented here, have been detected. About 50 of these occultations have been detected from only one or two different locations, which was not sufficient to

allow us to obtain the projected shape and size of the body. In these cases, it is always possible to derive astrometric positions (with very low uncertainties for the TNO) that can be used to improve their ephemerides (Rommel et al. 2020). To be able to fit the five parameters of an ellipse, at least three different observations are needed; otherwise, the problem is degenerate. The remaining 22 occultations (produced by 15 different TNOs), from the total of 77, were detected from more than two locations (i.e., multi-chord occultations). This allowed us to properly characterize their shapes and to derive very interesting and accurate physical properties. This means that we only obtained a good physical characterization using stellar occultations for about 15 TNOs, excluding Huya (see e.g., Elliot et al. 2010; Sicardy et al. 2011; Ortiz et al. 2012, 2017, 2020a; Braga-Ribas et al. 2013; Benedetti-Rossi et al. 2016, 2019; Dias-Oliveira et al. 2017; Souami et al. 2020, and references therein).

The stellar occultation by the TNO (38628) Huya presented here is the best ever stellar occultation by a TNO in terms of the number of chords obtained so far, excluding Pluto and the recent occultation by the TNO (307261) 2002 MS_4 on August 8, 2020 (Rommel et al., in prep). It is also the first multi-chord occultation reported for Huya.

The TNO (38628) Huya was discovered on March 10, 2000 from the Llano del Hato National Astronomical Observatory in Mérida (Venezuela) by astronomers of the Quasar Equatorial Survey Team (QUEST, Ferrin et al. 2001). Huya is classified as a plutino (i.e., it is in the 2:3 mean motion orbital resonance, MMR, with Neptune) and it is among the group of the ∼100 largest known TNOs; in fact, it is one of the biggest plutinos together with (119951) 2002 KX_{14}, (84922) 2003 VS_2, and (208996) 2003 AZ_{84}.

The infrared spectra of Huya appear moderately red and featureless, and they lack of any signatures of water ice or other volatiles (Jewitt & Luu 2001; de Bergh et al. 2004; Fornasier et al. 2013); however, other infrared spectra show faint signs of water ice (Barucci et al. 2011; Merlin et al. 2017). This points to a surface covered with a thick and red layer of dark organic compounds which would be homogeneously covered with trace amounts of water ice. Aqueously altered silicate minerals have also been proposed to explain some absorption features observed in the near-infrared spectra of Huya (Licandro et al. 2001; de Bergh et al. 2004). Besides spectra, colors from *Spitzer* Space Telescope at 3.6 and 4.5 µm have been modeled, indicating a surface composition of 40 ± 20% H_2O, 30 ± 10% silicates, and 30 ± 10% organics (Fernández-Valenzuela et al. 2021).

The rotational period of Huya is not well determined due to the small peak-to-peak amplitude of its light curve, however, a period of 6.75 ± 0.01 h was proposed by Ortiz et al. (2003) based on observations taken in February and March 2002. According to a more recent work by Thirouin et al. (2014), the period of 6.75 h could be an alias of Huya's rotation period that they propose (5.28 h) based on observations obtained from 2010 to 2013. Other alternative periods cannot be totally ruled out.

Huya has a known satellite provisionally designated as S/2012 (38628) 1, discovered by a team led by K. Noll in 2012 using images from *Hubble* Space Telescope (HST; Noll et al. 2012). The satellite's separation distance from the primary is estimated to be at least 1740 km.

The thermal emission from the Huya's system was measured with *Spitzer*/MIPS in 2004 and with *Herschel*/PACS and SPIRE in 2010. From these thermal data, using $H_V = 5.04 \pm 0.03$ mag, Fornasier et al. (2013) obtained an area-equivalent diameter for the system of $D_{eq} = 458 \pm 9$ km and a geometric albedo at V-band of $p_V = 0.083 \pm 0.004$. The area-equivalent diameter of Huya itself ($D_{Huya} = 406 \pm 16$ km) and its satellite ($D_{Satellite} \sim 213$ km), assuming the same albedo as Huya, were also obtained in that work. A summary of the orbital elements and most relevant physical characteristics of Huya from the literature is shown in Table 1.

In the present work, we analyzed the 21 chords obtained from the stellar occultation of the star *Gaia* DR2 4352760586390566400 ($m_G = 11.5$ mag) produced on March 18, 2019 by the TNO Huya. This paper is organized as follows. In Sect. 2, we describe the observations carried out to predict the occultation and the observations of the occultation itself. In Sect. 3, we detail the analysis of the Huya's occultation data. In Sect. 4, we describe the observations performed to refine the rotational period of Huya in order to determine the rotational phase at the moment of the occultation. In Sect. 5, the results obtained from the analysis of the occultation are given and discussed, including the instantaneous limb fit, the projected diameter, the 3D shapes, the albedo, the density, and the search for material orbiting Huya. Lastly, we present our conclusions in Sect. 6.

2. Observations

2.1. Predictions

Due to the wealth of information that can be obtained from stellar occultations by TNOs (e.g., Sicardy et al. 2011; Ortiz et al. 2012, 2017, 2020b,a, and references therein), we have been performing intensive astrometric and photometric observing campaigns since 2010 with the aim of predicting these events. This observing strategy has allowed us to derive accurate predictions (see Ortiz et al. 2020b, for a recent review).

Huya's orbit and ephemerides were derived using the Numerical Integration of the Motion of an Asteroid (NIMA, Desmars et al. 2015), a tool developed within the ERC Lucky Star project[1]. Part of the astrometric data of Huya used to feed NIMA were obtained with the 1.6-m telescope at Observatório Pico dos Dias (OPD) in Brazil on June 3, 2017 and July 8, 17, 2018. This telescope was equipped with an Andor IKon-L camera (2048 × 2048 pixels, field of view (FoV) = 6.1 × 6.1 arcmin, resolution = 0.18 arcsec/pixel), and a I-Johnson filter. In the course of these campaigns, we found that the TNO (38628) Huya would occult a V = 11.7 mag star (*Gaia* DR2 4352760586390566400, m_G = 11.5 mag) on March 18, 2019.

Around five months before the event, we refined the original NIMA's prediction using more astrometric data, as well as the data available in the Minor Planet Center database[2]. Near the occultation date, we once again refined the prediction based on images of Huya acquired with the 1.5-m telescope in Sierra Nevada Observatory (OSN) in Granada, Spain. This observing run was performed on March 2, 3, 8, 10, and 11, 2019 (around two weeks before the occultation event) with the 2k × 2k Andor IKON-L camera. 109 images were obtained in 2 × 2 binning mode at moon illumination < 20%. The detailed setup of these observations, including weather conditions and other related information, is shown in Table 2. Bias and sky flat-field frames were taken each night to calibrate the images.

The images obtained during the OSN observing campaign were astrometrically solved using *Gaia* DR2 (Gaia Collaboration 2016, 2018), which was the most precise astrometric catalog available when this occultation happened. The prediction was

[1] https://lesia.obspm.fr/lucky-star/
[2] https://www.minorplanetcenter.net/db-search

Table 1. Orbital and physical parameters of Huya from the literature.

Object	a (AU)	q (AU)	i (deg)	e	H_V (mag)	P (h)	Δm (mag)	Class.	$D_{\rm Huya}$ (km)	$p_{\rm V}$ (%)	$D_{\rm Satellite}$
(38628) Huya	39.69	28.55	15.47	0.28	$5.04 \pm 0.03^{(a)}$	$6.75 \pm 0.01^{(b)}/5.28 \pm 0.01^{(c)}$	$<0.1^{(b)}/0.02 \pm 0.01^{(c)}$	Plutino	$406 \pm 16^{(a)}$	$0.083 \pm 0.004^{(a)}$	$\sim$213 km$^{(a)}$

Notes. a: semi-major axis in Astronomical Units (AU), q: perihelion distance in AU, i: orbital inclination in degrees, and e: eccentricity, from Minor Planet Center (MPC-IAU) database, May 2021. H_V (mag): absolute magnitude at V-band. P (h): preferred single-peaked rotational periods. Δm (mag): peak-to-peak amplitude of the rotational light curves shown in the previous column. Class.: dynamical classification following Gladman et al. (2008) scheme. $D_{\rm Huya}$: area-equivalent diameter of Huya from radiometric technique, p_V: geometric albedo at V-band from radiometric technique, $D_{\rm Satellite}$: estimated diameter of the Huya's satellite from radiometric technique.
References: $^{(a)}$ Fornasier et al. (2013); $^{(b)}$ Ortiz et al. (2003); $^{(c)}$ Thirouin et al. (2014).

Table 2. Summary of the "last-minute" astrometric observing campaign.

Telescope	Date	CCD	Scale	FoV	Filter	Exp.	N	Seeing	S/N	1σ (RA)	1σ (Dec)	Offset (RA)	Offset (Dec)
OSN 1.5-m	March 2,3,8,10,11, 2019	2k × 2k	0.46″/pix	7.5′ × 7.5′	R-Johnson	400 s	109	1.6”	45	8 mas	8 mas	149 mas	–92 mas

Notes. Telescope is the telescope used during the observing run. Date refers to the observing dates. CCD is the size of the Andor IKON-L detector. Scale is the binned image scale of the instrument. FoV is the field of view of the instrument. Filter is the filter used. Exp. is the exposure time of the individual images. N is the total number of images. Seeing is the average seeing during the observing runs. S/N is the signal to noise ratio of the object. 1σ (RA) is the average 1σ uncertainty in right ascension (RA) of the astrometry in milliarcseconds (mas). 1σ (Dec) is the average 1σ uncertainty in declination (Dec) of the astrometry in mas. The Offset (RA) and Offset (Dec) are the offsets for right ascension and declination with respect to the JPL#28 orbit expressed in mas.

obtained using the coordinates of the occulted star (*Gaia* DR2 4352760586390566400) propagated to the occultation epoch using the *Gaia* DR2 proper motions and parallax, as well as the relative astrometry (offsets) of Huya with respect to the Jet Propulsion Laboratory orbit JPL#28. The average 1σ astrometric uncertainties obtained and the offsets with respect to the orbit JPL#28 are shown in Table 2. These uncertainties translate to 1σ uncertainties of 165 km projected on Earth surface (cross-track) and 20 s in time (along-track). The final prediction map obtained is shown in Figure 1. We note that the center line of the shadow path of this final prediction is ~3000 km east of the prediction based only on the JPL#28 orbit of Huya and the *Gaia* DR2 position of the star and ~1900 km west of the prediction obtained about five months before the event. The width of the shadow path in this Figure is assumed to be the diameter of Huya derived from *Herschel* and *Spitzer* thermal data ($D = 406$ km, according to Fornasier et al. 2013). The real shadow path of the occultation was ~78 km west of the final prediction (see Fig. 2) but within the estimated uncertainties.

As the "last-minute" prediction from the OSN telescope (see Table 2) was favorable to many countries in Europe and involved a bright star, we alerted our (previously notified) European collaborators, stressing the importance of observing this occultation. In total, 21 positive detections from 18 sites longitudinally distributed and 16 misses were obtained.

Fig. 1. Last-minute prediction of the occultation using *Gaia* DR2 star catalog (Gaia Collaboration 2016, 2018) and relative astrometry of Huya regarding the occulted star obtained from the 1.5-m telescope in Sierra Nevada Observatory, Granada, Spain. The green line indicates the centrality of the shadow path and the blue lines the limits of the shadow assuming an area-equivalent diameter for Huya of 406 km (Fornasier et al. 2013). The 1σ precision along the path is 165 km and the 1σ precision in time is 20 s. The arrow in the right bottom shows the direction of the shadow motion[3].

2.2. Stellar occultation

On March 18, 2019, a total of 49 telescopes located in Europe and Asia (Israel) were ready to observe the occultation by the TNO Huya. Because we alerted the community of amateur occultation observers through the "planoccult" list, some of the telescopes were located too far from the nominal prediction (e.g., Spain, UK, Eastern Turkey) to allow for the detection of the Huya satellite or any possible rings. Time series of images or video observations were acquired with 37 of these telescopes (from the other 12, there were 8 that were subject to bad weather and 4 suffered technical problems). Video observations were converted to FITS images prior to their analysis using same procedures and precautions adopted in Benedetti-Rossi et al. (2016). From 21 of the 37 telescopes, located at 18 different sites, we recorded the occultation of the star produced by Huya. From 16 of the 37 telescopes, the occultation was not detected. All stations and telescopes that recorded a positive detection plus two very close stations which missed the occultation (QOS Observatory

[3] Map credit: https://www.gpsvisualizer.com/ and Australian Topography (©Commonwealth of Australia – Geoscience Australia – 2016. Creative Commons Attribution 4.0 International License).

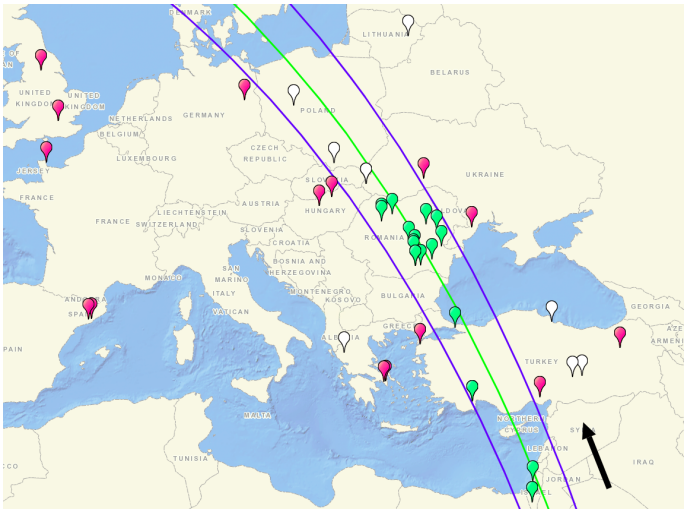

Fig. 2. Map of post-occultation shadow path of the stellar occultation by Huya, the path width (limited by the blue lines) is the area-equivalent diameter obtained from the reconstructed ellipse fit ($D = 411.3$ km, see Sect. 5.1). The site positions from where the occultation was recorded are shown with green marks, the negative detections with red marks, and the sites that did not observe due to bad weather or to technical problems are indicated with white marks. The green line indicates the centrality of the shadow path and the blue lines the limits of the shadow. The arrow in the right bottom shows the direction of the shadow motion[3].

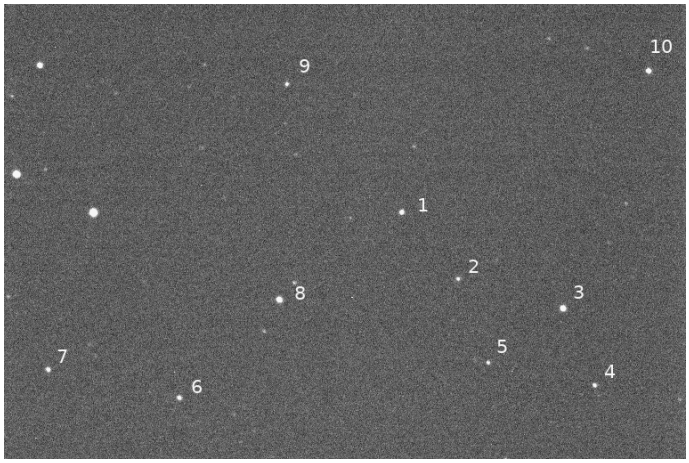

Fig. 3. One of the images of the occultation obtained from the Astronomical Observatory Cluj-Napoca in Romania (see Table A.1 for details). The source marked as "1" corresponds to the occulted star plus Huya before the beginning of the occultation. The other marked sources were used as reference stars. The FoV of the image is 20×13 arcmin, north is up and east is to the left.

in Ukraine and Çukurova University Observatory in Turkey) are listed in Table A.1. Basic information about the 49 telescopes that participated in this campaign and their locations is shown in the online Table A.2.

Aperture photometry for each data set was obtained, from which we derived the light curves (flux of the star normalized to the mean value before the occultation versus the time). The light curves from the 21 positive observations at 18 sites (see Table A.1) showed drops in flux caused by the occultation. Light curves from the other 16 telescopes that did not detect the occultation were also obtained and carefully analyzed. We analyzed with special care the negative detection at QOS Observatory in Zalistci (Ukraine), which was the closest to the shadow path. This closer non-detection provides an opportunity to notably constrain the projected shape edge of Huya (see Fig. 2 and Table A.1).

The time in all the observing sites was synchronized via network time protocol servers (NTP) or GPS-based video time inserters (VTI). Each image header includes the acquisition time. Most of the series of images were obtained with around 10–15 min before the predicted occultation time up to around 10–15 min after the event. This strategy allowed us to have a good characterization of the photometric baseline and to probe the surroundings of the object (i.e., the presence or absence of satellites, rings, or other orbiting material). No filters were used in any of the telescopes in order to maximize the signal to noise ratio (S/N) of the occulted star with the aim to obtain the best possible photometric data.

The light curves of the occultation were obtained using our own IDL (Interactive Data Language) codes based on DAOPHOT routines and using the PRAIA photometry tool (Assafin et al. 2011) after the usual dark, bias, and flat-field corrections when calibration images were available. Then, the relative photometry of the occulted star was obtained on the images using the stars present in the FoV as comparison stars with the aim of minimizing flux variations due to atmospheric transparency fluctuations and to different seeing conditions. We used as many reference stars as possible from 3 to ~25 depending on the FoV (see Fig. 3). In some cases, the observers only read a Region of Interest (RoI) of the detector to minimize the readout time; in these cases, the FoV was smaller (i.e., a smaller number of reference stars) than the FoV from other telescopes. We did not use the same reference stars for different data sets, as the number of stars within the FoV was different from telescope to telescope. In the end, the flux of the occulted star is compared to an ensemble mean of all the selected reference stars. The chosen aperture diameters, starting with diameters around the full width at half maximum (FWHM), minimized the flux dispersion of the occulted star before and after the occultation.

It is important to note that the flux of the occulted star obtained during the occultation is the combination of the flux of the star and the flux of Huya, although in this case, the flux of Huya has a very small contribution (~0.07%) to the total flux due to the brightness of the occulted star. Finally, the light curve (i.e., the combined flux of the occulted star and Huya versus time) was obtained for each data set. The light curves obtained from the 21 telescopes that detected the occultation show deep dimmings in flux at the expected occultation times (Fig. 4). Detailed information about the sites, telescopes, detectors, exposure times, observers, and light curves dispersion, from which the occultation was detected is shown in Table A.1. This table also includes information about the two stations closest to the shadow path that reported a negative detection (QOS Observatory in Ukraine and Çukurova University Observatory in Turkey). More details and complementary information on the analysis of these occultation light curves are given in Sect. 3.

3. Analysis of the stellar occultation by Huya

The TNO (38628) Huya occulted the $m_G = 11.5$ mag star *Gaia* DR2 4352760586390566400 on March 18, 2019 at ~00:53 UTC. The typical sampling times were greater than 0.2 seconds (i.e., ≥1.61 km in the body plane of Huya), this means that our data are dominated by the exposure times rather than by the Fresnel diffraction effects (≃1.13 km) or the stellar diameter

Table 3. Details of the occulted star and other occultation related information.

Designation	*Gaia* DR2 4352760586390566400
Coordinates DR2[(a)]	α = 16h41m06.4260s, δ = –06°43′34.″5756
Star position errors[(b)]	errRA = 0.1474 mas, errDec = 0.1143 mas
Proper motions & Parallax[(c)]	pmRA = –4.506 ± 0.090 mas yr^{-1}, pmDec = –14.340 ± 0.055 mas yr^{-1}, Plx = 1.5717 ± 0.0478 mas
Magnitudes[(d)]	B = 12.296, V = 11.751, R = 11.380, J = 10.541, H = 10.384, K = 10.294, G = 11.538
Star Diameter[(e)]	~0.0342 ± 0.0014 mas (~0.70 ± 0.03 km at Huya's distance)
Fresnel[(f)]	1.13 km
Exposure time effect[(g)]	1.61 km
Velocity[(h)]	8.07 km s^{-1}

Notes. [(a)]*Gaia* DR2 coordinates propagated to the occultation epoch (2019.211) using the proper motions and parallax. [(b)]errRA and errDEc are the errors in RA and Dec from the *Gaia* DR2 catalog propagated to the occultation epoch using the formalism by Butkevich & Lindegren (2014). This formalism has been applied using the SORA tool (Gomes-Júnior et al. 2022). [(c)]pmRA and pmDec are the proper motions in RA and Dec and respective errors, Plx is the absolute stellar parallax with error. [(d)]B, V, R, J, H and K from the NOMAD catalog (Zacharias et al. 2004). G from the *Gaia* DR2 catalog (Gaia Collaboration 2018). [(e)]Size estimated using V and K magnitudes and the van Belle (1999) equation for a main sequence star. [(f)]Fresnel diffraction effect: F = $\sqrt{\lambda d/2}$, with d = 28.3500 AU at the occultation moment and λ = 600 nm. [(g)]Smallest exposure time from the positive detections multiplied by the event shadow velocity. [(h)]Velocity of Huya with respect to the star as seen from Earth.

(≃0.70 km at Huya's distance). The Fresnel scale value of $F = \sqrt{\lambda d/2} = 1.13$ km is obtained from the geocentric distance of Huya during the occultation ($d = 28.3500$ AU) and the average central wavelength of the observations ($\lambda = 600$ nm). To estimate the angular diameter of the occulted star we use its V (11.751 mag) and K (10.294 mag) apparent magnitudes from the NOMAD catalog (Zacharias et al. 2004) as well as the van Belle (1999) equation for main sequence stars, obtaining a diameter of ≃0.0342 mas (≃0.70 km at Huya's distance). Table 3 summarizes the occulted star details and other related information.

The light curves obtained from the stellar occultation (see Figure 4) are used to derive the times of disappearance ("ingress" time) and reappearance ("egress" time) of the star behind the Huya's limb. These ingress and egress times can be directly translated to distances in the plane of the sky using the apparent motion of Huya relative to the occulted star, which is 8.07 km s^{-1} for this occultation (see Table 3). The derived segments in the plane of the sky are known as "chords". From these chords, we can obtain the physical properties described in Sect. 5. The times of disappearance and reappearance and their uncertainties at each site are obtained creating a synthetic light curve by using a square-well model convolved with the Fresnel scale, the star apparent size and the exposure time (Elliot et al. 1984; Roques et al. 1987). The parameters fitted are the ingress and egress times and the depth of the occultation. The difference between the data and the synthetic light curve is iteratively minimized using a χ^2 metric. This technique is described in detail in Ortiz et al. (2017) and Benedetti-Rossi et al. (2019), and the references therein.

The ingress and egress times and their associated uncertainties obtained in this way are shown in Table A.3. These times determined 20 chords of different sizes in the plane of the sky also included in Table A.3. Due to a CCD camera failure the ROASTERR-1 Observatory (Romania) missed the ingress. As a consequence, only the egress time is considered for this observatory (see light curve #4 in Fig. 4). In the end, 19 chords obtained from the 21 telescopes that detected the occultation in Table A.1 were used to obtain the results described in Sect. 5: (i) the chord from the Amateur Observatory-3 in Romania (AO-3) is not used because the absolute time information of this chord was missed, there was no timestamp in images and no time in image headers, this means that we only have relative timing, we used the reference time for the first frame of 00:00:00.0 UTC and we derived the chord size with its associated error bars; (ii) the light curves obtained from Galați Observatory-1 and Galați Observatory-2 in Romania were obtained at the same site with the same integration time, so we merged the two data sets in order to have a single light curve and chord (#18) with more data during the occultation.

4. Rotational light curve of Huya

To obtain the rotational phase of Huya at the moment of the occultation, we used the already published photometry of 299 images acquired in 2010–2013 with the 1.5-m OSN telescope in Granada (Spain) and with the 1.23-m telescope at Calar Alto Observatory in Almería (Spain), see Thirouin et al. (2014) for further details about these observations. We merged these data with 116 new images of Huya acquired over eight nights in 2019 on July 1–4 and August 1–4 (~3–4 h of observation each night), with the 1.5-m OSN telescope with integration times of 400 seconds, binning of 2 × 2, and no filter in order to achieve the highest S/N.

Standard bias and flat field corrections were applied to all the images before the extraction of the fluxes of the object and of the selected comparison stars by means of an aperture photometry technique. To perform this task, we used specific routines coded in IDL, trying different values for the apertures (starting with apertures around the FWHM) and sky ring annulus for the object and the same values for the comparison stars in order to maximize the S/N of the object and to minimize the dispersion of the photometry. When possible, we choose the same set of comparison stars for all nights within the observing run to minimize systematic photometric errors. The data processing used was the same as that described in detail in, for instance, Fernández-Valenzuela et al. (2016).

The final product obtained is the flux of Huya respect to the comparison stars versus time (corrected for light travel times). A Lomb-Scargle technique (Lomb 1976) was applied to these time series data in order to obtain the rotational period of Huya. The rotation period with the highest spectral power obtained from the Lomb-Scargle periodogram is 6.725 ± 0.006 h (Fig. 5), which is compatible with other published rotation periods (e.g., Ortiz et al. 2003; Thirouin et al. 2014). Aliases of this period,

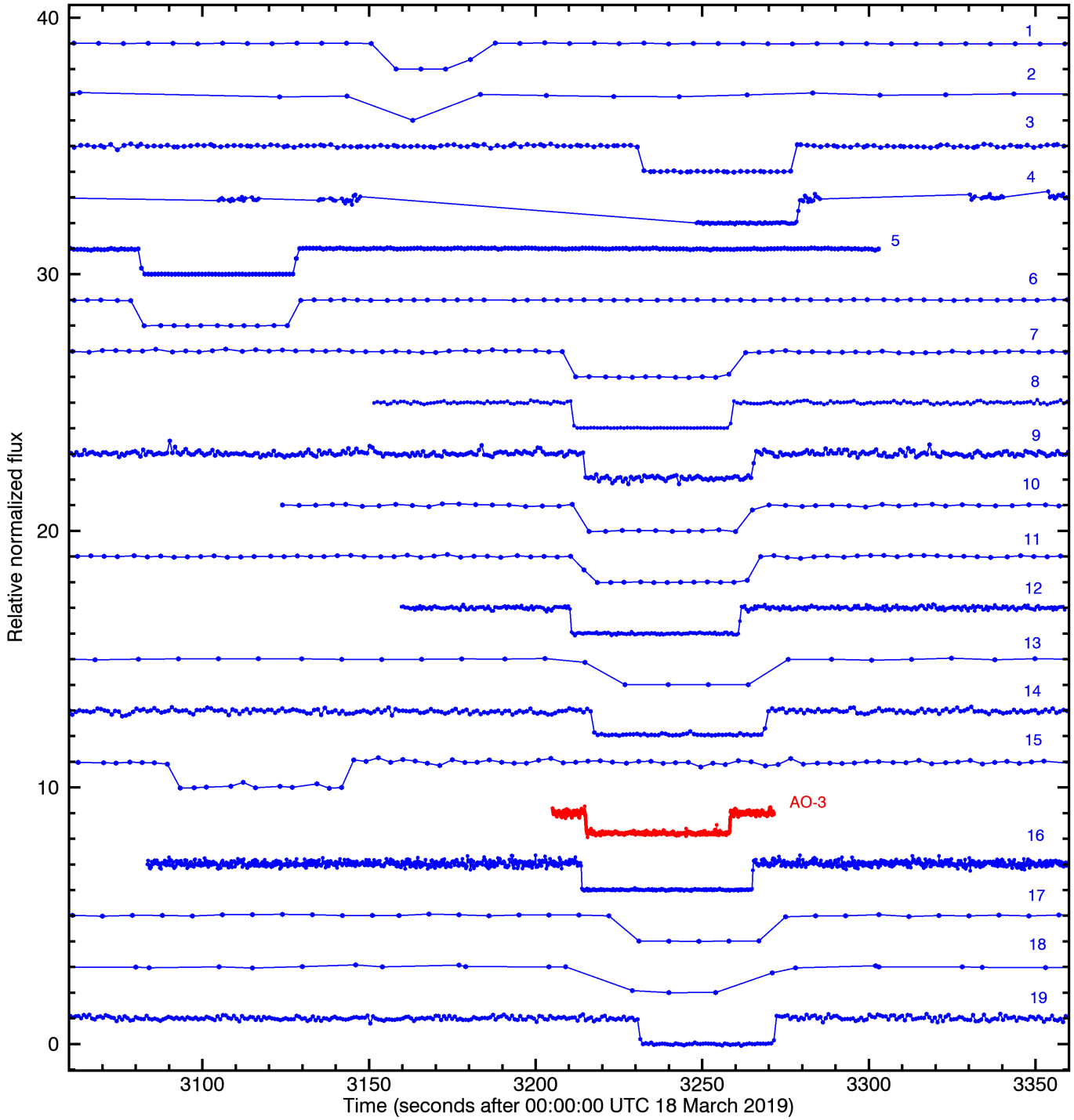

Fig. 4. Stellar occultation light curves (normalized flux versus time) from the 21 positive detections, as presented in Table A.1. Each individual measurement is indicated with a dot, with these measurements connected by a solid line for clarity. The light curves are shifted in flux for a better viewing and are presented from top to bottom with respect to their distance to the center of the predicted shadow path, from west to east. Flux uncertainties are not shown in order to avoid an unreadable plot (the standard deviation of the measurements are indicated in Table A.1). Chord #18 is the combination of two light curves obtained from the same site (Galați Observatory, Romania) with two telescopes of 40-cm and 20-cm, respectively. The light curve in red (AO-3) was not used to obtain the limb fit, it has been shifted in time to properly appear in this plot because the time information of this chord was missed.

such as ~5.2 h or ~4.3 h, cannot be excluded, as is shown in the bottom panel of Fig. 5.

This updated rotational light curve allows us to determine the rotational phase at the moment of the occultation and it turns out that Huya was near one of its absolute brightness minima at the time of the occultation on March 18, 2019. This means that the TNO occulted the star when its apparent surface area was near its minimum. The rotational light curve in the upper panel of Fig. 5 is fitted with a Fourier function in order to derive the peak-to-peak amplitude of the light curve, which results to

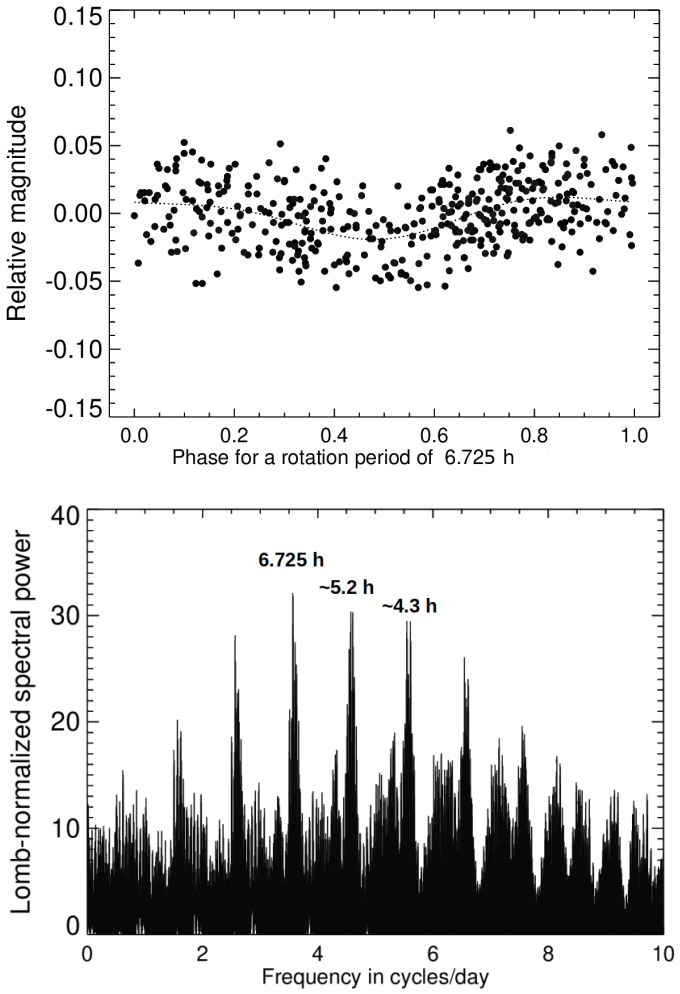

Fig. 5. Possible rotational periods of Huya discussed in this work. *Top panel:* Rotational light curve (relative magnitude vs. rotational phase) of Huya obtained from the data described in Sect. 4. The data have been folded with a rotational period of 6.725 h. The zero rotational phase in the plot is fixed close to the moment of the occultation (March 18, 2019 00:54:00 UTC). *Bottom panel:* Lomb periodogram showing the rotational period $P = 6.725$ h, which corresponds to the peak with the highest spectral power. The two other aliases at high spectral power correspond to other possible rotational periods of Huya: $P \sim 5.2$ h and $P \sim 4.3$ h.

be of 0.031 ± 0.005 mag. This amplitude is slightly larger than the previously published amplitudes (Ortiz et al. 2003; Thirouin et al. 2014). The zero rotational phase in the upper panel of Fig. 5 was chosen to be the moment of the stellar occultation (i.e., on March 18, 2019 00:54:00 UTC).

Alternatively, the very shallow rotational light curve obtained could be directly related to the rotation of the satellite of Huya, as it is suspected to be the case for the TNO 2002 TC_{302} (Ortiz et al. 2020a). If Huya's satellite has a very irregular shape, it could cause a shape-driven light curve which would dominate the rotational light curve of the system; this would also be consistent with a very round shape for Huya (Maclaurin spheroid). On the other hand, a rotational period of 6.725 h would indeed be an unusual period for a satellite, because a rotation period synchronized with its orbital period is expected, which would be of days, not of hours. However, we know that Haumea's largest satellite, Hi'iaka, has a much faster rotation period (~9.8 h) than its orbital period (~49.5 days) according to Hastings et al. (2016). A binary system with a mass ratio of the satellite to the main body similar to the Huya system is Varda-Ilmarë (mass ratio ~9%). In this system, it is likely that the rotation of the main body, Varda, is not synchronized with the mutual orbital period. This can be explained by the fact that the estimated time scale for synchronization is longer than the age of the solar system (Grundy et al. 2015). Similar calculations can be performed when the orbit of the Huya's satellite becomes available, which would shed light on whether or not its rotation is synchronized with its orbital period, and whether this potential lack of synchronization is common in TNO satellites.

5. Results

The obtained physical properties of Huya, namely, its projected shape, the size, the geometric albedo, and the 3D shape (shown in Sects. 5.1 and 5.2) were determined from the chords presented in the previous section. In Sect. 5.3, we characterize the environment around Huya and possible rings or debris orbiting this plutino are constrained. Finally, in Sect. 5.4, we place constrains on a putative atmosphere around Huya.

5.1. Projected shape, diameter, and albedo of Huya

From the 19 chords numbered in Table A.3, we have 37 chord extremities that can be used to obtain the projected shape (i.e., the instantaneous limb) of Huya at the moment of the occultation. These extremities give the position (f, g) of the star projected in the sky plane of the body and relative to the center of the object. f and g are counted positively toward local celestial east and celestial north, respectively, and are measured in kilometers (see, e.g., Benedetti-Rossi et al. 2019). We note that we have 37 instead of 38 extremities because we discard the ingress time of the ROASTERR-1 Observatory in Romania (chord #4), which was missed due to a CCD camera failure. The closest negative chord from QOS Observatory in Ukraine is also used to constrain the limb. We fitted an ellipse to these 37 points as described below.

The best-fitting ellipse was obtained through a χ^2 minimization method applied to the 37 chord extremities. The function to minimize is $\chi^2 = \sum_{i=1}^{37}(r_{i,\rm obs} - r_{i,\rm com})^2/\sigma_{i,\rm r}^2$, where r is the radius from the center of the ellipse $(f_{\rm c}, g_{\rm c})$, the subscripts "obs" and "com" means observed and computed, respectively, and $\sigma_{i,\rm r}$ are the errors on the extremities determination. What we finally obtain from this fit are the apparent or projected semi-axes of the ellipse (a', b'), the center of the ellipse $(f_{\rm c}, g_{\rm c})$ and the position angle of the minor axis of the ellipse (P'), namely, the apparent position angle of the pole measured eastward from celestial north. Since the ellipse fit is not linear in the parameters, an estimate of the error in the parameters using a χ^2 minimization technique may result in an underestimation of the errors. Therefore, we estimated the uncertainties in the five parameters of the fitted ellipse using a Monte Carlo approach, as done in Santos-Sanz et al. (2021). We randomly generated the 37 chord extremities 10^4 times, meeting the requirements provided by their corresponding uncertainties. For each one of these sets of randomly generated extremities, we obtained the best-fitting ellipse in terms of a minimization of the sum of squared residuals $\sum_{i=1}^{37}(r_{i,\rm obs} - r_{i,\rm com})^2$, where $r_{i,\rm obs}$ and $r_{i,\rm com}$ are the same as described above. In the end, we had 10^4 best-fitting ellipses to the 37 randomly obtained extremities (i.e., 10^4 possible values of the five parameters that determine an ellipse: a', b', $f_{\rm c}$,

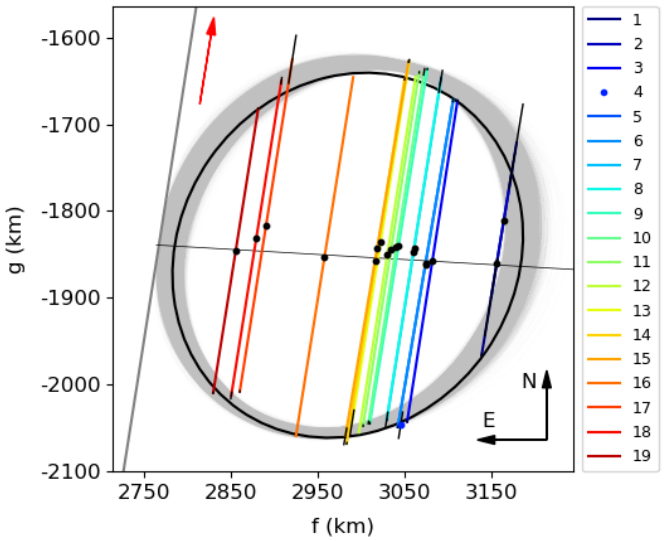

Fig. 6. Best-fitting ellipse (in black) to the 19 chords presented in Table A.3 (for chord #4 only egress time is used). The fitted ellipse determines the projected shape of Huya at the moment of the occultation and has axes of 435.2 ± 7.0 km $\times$ 388.2 ± 12.2 km. The gray ellipses are the best-fitting ellipses to the 10^4 randomly generated chord extremities (see Sect. 5.1 for details). The black dots are the centers of the chords, and the gray line crossing all the chords is a weighted linear fit to these dots. The black solid lines in the extremities of the chords are the 1σ uncertainties of the ingress and egress times. The red arrow shows the direction of the shadow motion. The chord numbers are the same as those used in Tables A.1 and A.3 and Fig. 4. The negative detection at QOS Observatory in Ukraine (light gray line at the left of the ellipse) helps to constrain the limb fit.

g_c, and P'). From these parameter distributions, we obtained the 1σ uncertainty in each parameter as the standard deviation of the corresponding distribution (see Table A.4 and Fig. 6).

The parameters and uncertainties obtained for the best-fitting ellipse, as explained above, are (f_c , g_c) = (2984.7 ± 3.2 km , −1850.9 ± 1.7 km), (a' , b') = (217.6 ± 3.5 km , 194.1 ± 6.1 km), and $P' = 55.2° \pm 9.1$. The axes ratio of this ellipse is small and close to 1.0 ($a'/b' = 1.12 \pm 0.05$), which indicates that Huya is a very round object, as shown in Fig. 6 where the 19 chords (only egress for chord #4) and their uncertainties obtained from the occultation are plotted in the plane of the sky together with the best-fitting ellipse to their extremities. We note that the center obtained from the elliptical fit (f_c , g_c) provides the offsets with respect to the positions of Huya obtained using the Jet Propulsion Laboratory orbit JPL#28 + Development Ephemeris model DE431, assuming that the *Gaia* DR2 occulted star position is correct. As shown in Fig. 6, the centers of the chords were not well aligned and their extremities were not always well fitted by the best-fitting ellipse. On the other hand, an ellipse would be the expected projected shape for Huya considering that an icy body with its size should have adopted a regular equilibrium figure with only minor irregularities due to topography (see discussion in Sect. 5.2). If this is true, the chords centers must be aligned (see, e.g., Braga-Ribas et al. 2013; Santos-Sanz et al. 2021). For completeness, and to check whether this solution is very different from the original one, we slightly shifted the chords by performing a linear fit to the centers of the chords and looking for the ellipse that best fits these chords. The semi-axes obtained for the best-fitting ellipse to the shifted chords were (a', b') = (220.2 ± 4.3 km , 197.4 ± 6.1 km), which differ by less than 2% concerning the unshifted solution. Since both solutions (the original and the shifted) are virtually the same, we decided to use the best-fitting ellipse to the original (unshifted) chords as the best solution, since no a priori assumption is made about the centers of the chords in the latter.

From the limb fit to the original chords we derived an area-equivalent diameter of Huya at the moment of the occultation of $D_{eq} = 411.0 \pm 7.3$ km. If Huya is a triaxial body, this diameter is a lower limit of the total area-equivalent diameter of this plutino because (as shown in Sect. 4) Huya was very close to its absolute brightness minimum at the moment of the occultation; that is, its projected area was very close to its minimum. If Huya is an oblate Maclaurin-like body, this diameter will be the real projected diameter and the rotational light curve should be due, in this case, to albedo variations in the surface. In any case, this diameter is smaller than the radiometric area-equivalent diameter obtained using *Herschel* (PACS and SPIRE) and *Spitzer* (MIPS) measurements: $D_{eq} = 458 \pm 9.2$ km (Fornasier et al. 2013).

However, to do a proper comparison of the occultation and radiometric diameters, we have to take into account that the radiometric diameter includes the thermal flux of Huya and its satellite since neither the *Herschel* Space Observatory nor *Spitzer* Space Telescope can resolve the Huya's system. Fornasier et al. (2013) did an estimation of the equivalent size of the main body and the satellite from radiometric models (assuming same geometric albedo for both bodies), obtaining a measurement of $D_{Main} = 406 \pm 16$ km and $D_{Satellite} = 213 \pm 30$ km. This means that the area-equivalent diameter of Huya obtained from the occultation is slightly bigger (411.0 km) than the radiometric-derived one (406 km), but both diameters are fully compatible within their error bars. This underestimation in the radiometric diameters has been noted for other TNOs when properly comparing occultation diameters with radiometric ones (Ortiz et al. 2020a,b).

From the best-fitting ellipse, we derived the geometric albedo at V-band of the Huya's surface at the moment of the occultation by means of the equation (Sicardy et al. 2011):

$$p_V = 10^{0.4(V_{sun} - H_V)}/(A/\pi), \quad (1)$$

where V_{sun} is the V-magnitude of the Sun (V_{sun} = -26.74 mag), H_V is the absolute magnitude of Huya at V-band, and A is the projected area of the TNO (expressed in AU^2) directly obtained from the occultation limb fit.

It is important to highlight that the absolute magnitude provided for Huya in the literature is that of the Huya's system (i.e., the combined magnitude of Huya and its satellite). To obtain the absolute magnitude of Huya itself we used the difference in optical magnitude between Huya and its satellite measured by Noll et al. (2012), which is ~1.4 mag. Using this difference, and assuming $H_V = 5.04 \pm 0.03$ mag for the Huya's system from Fornasier et al. (2013), we obtained an absolute magnitude of $H_V = 5.31$ mag for Huya. Finally, to obtain the albedo, we have to correct this value of H_V by taking into account the rotational phase at the moment of the occultation. The object was close to its minimum projected area during the occultation (Sect. 4), which means that we should add $\Delta m/2 = 0.031/2$ mag = 0.016 mag to H_V to derive the absolute magnitude of Huya at the moment of the occultation, obtaining $H_V = 5.326$ mag. Using the latter value for H_V, we obtained a geometric albedo of $p_V = 0.079 \pm 0.004$ for Huya. This albedo is smaller than the albedo derived from the radiometric method using *Herschel* and *Spitzer* thermal data ($p_V = 0.083 \pm 0.004$, from Fornasier et al. 2013), but the radiometric albedo was computed for the Huya's system.

5.2. 3D shape models for Huya

In what follows, we assume fluid-like behavior for Huya, as is commonly done for TNOs (see, e.g., Thirouin et al. 2010; Duffard et al. 2009) and we used the Chandrasekhar formalism (Chandrasekhar 1987) to obtain possible Maclaurin or Jacobi equilibrium shapes for this TNO.

In general, TNOs with shallow rotational light curves ($\Delta m \leq 0.15$ mag) are associated with Maclaurin-like shapes (Sheppard & Jewitt 2002; Ortiz et al. 2003; Duffard et al. 2009). In this case, the variability is produced by albedo marks on the surface of the object, and the rotational light curves will be single-peaked. For larger peak-to-peak amplitudes ($\Delta m > 0.15$ mag) a Jacobi ellipsoid shape is expected. In this case, the rotational light curve is shape-driven, presenting a double-peaked shape. We believe that most (~75%) of the large TNOs ($D > 300$ km) have Maclaurin spheroid shapes, rather than triaxial ellipsoid shapes (Duffard et al. 2009).

According to Tancredi & Favre (2008), Huya has enough size to reach hydrostatic equilibrium. We also know from the statistics of rotational periods and amplitudes of TNOs, most of which are the size of Huya or even smaller, that hydrostatic equilibrium shapes reproduce that statistic well (see, e.g., Duffard et al. 2009). This is a clear indication that not only Huya but also other smaller TNOs seem to be compatible with hydrostatic equilibrium. One of the reasons could be that the mechanical properties of the internal material are probably weaker than those of water ice, perhaps due to porosity or other effects (see, e.g., Thirouin et al. 2010). Then, under this equilibrium assumption, a Maclaurin spheroid with semi-axes a, b, and c ($a = b > c$, where c is the rotation axis) is the most likely 3D shape for this TNO, taking into account the single-peaked and shallow ($\Delta m = 0.031$ mag) rotational light curve presented by this body (see Sect. 4 and Fig. 5). Therefore, we explored possible Maclaurin shapes compatible with the rotational light curve and with the results obtained from the occultation. According to Bierson & Nimmo (2019) and from Fig. 3 in Grundy et al. (2019), the expected density for a TNO with $D \sim 410$ km is $\rho < 800$ kg m^{-3}. A Maclaurin spheroid with this density rotating with a period of 6.725 h (i.e., the preferred one discussed in Sect. 4) would have semi-axis ratios $a/c = b/c = 1.87$. The aspect angle[4] needed to obtain, from this Maclaurin, the projected axial ratio obtained from the occultation ($a'/b' = 1.12$) is 32°, which is a very small aspect angle. We note that for a random distribution of spin axes, the most likely aspect angle is 60° and the typical probability density distribution goes with the sine of the aspect angle. The likelihood of aspect angles 32° or smaller is ~15%. This probability is not too small, but it means it is not very likely.

If Huya's satellite is in the equatorial plane, the tilt angle of the orbit will allow us to determine the aspect angle. Huya's satellite orbit is not available yet although it should be ready soon (Grundy, priv. comm.). However, with the data we currently have, a Maclaurin spheroid with $\rho \sim 800$ kg m^{-3} compatible with the occultation and with the preferred rotational period ($P = 6.725$ h) would have axes: $2a = 435$ km, $2b = 435$ km, $2c = 233$ km, for an aspect angle of 32°. For the other possible and shorter rotation periods ($P \sim 5.2$ h and $P \sim 4.3$ h), the aspect angle should be even smaller (<30°), which is more unlikely (probability ~13%).

Alternatively, we can assume that the rotational light curve of Huya is produced by a rotating triaxial ellipsoid (i.e., a Jacobi ellipsoid) with semi-axes a, b, and c ($a > b > c$, with c the axis of rotation). The minimum density expected for a Jacobi ellipsoid rotating with $P = 6.725$ h is $\rho = 859$ kg m^{-3}. The aspect angles compatible with the occultation ($a'/b' = 1.12$) and with the rotational light curve ($\Delta m < 0.031$ mag) span from 31° to 43°. For these aspect angles, a family of Jacobi solutions rotating at 6.725 h with $\rho_{\rm min} = 859$ kg m^{-3} is possible: $2a = [440–455]$ km, $2b = [428–442]$ km, $2c = [253–261]$ km. On the other hand, the minimum density required for a Jacobi rotating with $P \sim 5.2$ h is $\rho = 1440$ kg m^{-3}, a very large density for a body of the Huya's size. A Jacobi ellipsoid rotating with $P \sim 4.3$ h would require an even larger and unlikely minimum density ($\rho = 2100$ kg m^{-3}).

An alternative three-dimensional shape solution to a Maclaurin (close to pole-on) or Jacobi (with too high densities) shapes invokes non-hydrostatic equilibrium shapes, via granular media or differentiation (the latter unlikely for Huya's size), which would not need so high densities. The exploration of these non-hydrostatic solutions is beyond the scope of this paper.

5.3. Probing Huya's environment

We did not detect secondary drops below the 3σ level of noise in the positive occultation light curves related to the satellite or possible rings around Huya (Fig. 4). Secondary drops below the 3σ level were also not detected in the negative light curves. We can constrain the presence of rings (or debris) around Huya using the light curves obtained during the occultation (e.g., Braga-Ribas et al. 2014; Ortiz et al. 2017; Sickafoose et al. 2019; Santos-Sanz et al. 2021).

For a given exposure time in seconds ($t_{\rm exp}$), and a measured photometric uncertainty (σ), for the event velocity v ($v = 8.07$ km s^{-1} for the occultation by Huya) at a significance of 3σ, the minimum detectable ring width is $w = t_{\rm exp} v$. Opacity variations can be detected at the 3σ level, where op $= 3\sigma$. For other opacities (op), the minimum width (w) of a ring detectable at 3σ can be obtained as $w = 3\sigma t_{\rm exp} v/{\rm op}$.

The best positive occultation light curve, in terms of flux dispersion, was obtained from the C18 telescope at the Wise Observatory data (see Table A.1) with $\sigma_{\rm flux} = 0.009$. The minimum opacity of a putative ring detectable at 3σ using this light curve is 2.7% for a ring width of 24.2 km. In other words, a ring with a width ≥24.2 km and an opacity ≥2.7% would produce a drop in the light curve easily detectable below the 3σ level of noise. If the opacity of the ring were 50%, we could have detected rings with a width ≥1.3 km at 3σ. For an opacity of 100% a ring with a width ≥0.7 km could have been detected below the 3σ level (see Table A.5). The latter constraints on the ring's width were obtained without take into account the dead-time during the data acquisition, which was of 1.46 s for the C18 at Wise Observatory. This means that rings with widths of ≤11.8 km could have been lost during the dead-times. The other positive occultation light curve obtained at the same observatory with the W-FAST telescope (Nir et al. 2021) has a very short dead-time of only 0.007 s (maximum ring width during dead-time = 0.06 km) with also a small dispersion in flux ($\sigma_{\rm flux} = 0.015$). Therefore, from this data we could have detected rings at the 3σ level of noise with widths ≥0.7 km for an opacity of 50% and with widths ≥0.4 km for an opacity of 100%, in both cases, with negligible ring width losses during the dead-times (≤0.06 km).

We obtained constraints at the 3σ level on the ring sizes for the other positive light curves and the closest negative one for the minimum opacity and for opacities of 50% and 100%. The derived constraints are shown in Table A.5. The

[4] We consider that the aspect angle is 0° if the object is in a pole-on geometry and 90° for an equator-on geometry.

best constraint, in terms of ring width, was obtained from the Amateur Observatory-3 in Romania, with integration times of 0.0333 s (without dead-times) and $\sigma_{\rm flux} = 0.074$, from where rings with widths ≥0.1 km for an opacity of 50% could have been detected at the 3σ level of noise.

From all the above, we can conclude that no debris or rings of the type found in the dwarf planet Haumea (opacity ∼50%, Ortiz et al. 2017) have been detected around Huya through this stellar occultation. However, narrow (≤0.1 km) and optically thin rings (opacity ≤50%) at different geometries, not probed by the occultation light curves, cannot be ruled out. We also note that diffraction effects will be important for rings with a width < 1.13 km (the Fresnel scale value) and high opacity.

5.4. Setting constraints on a putative atmosphere

Assuming that Huya is a predominantly icy body, we attempted to place constraints on a possible atmosphere. The sublimation rate of water ice is extremely low at Huya's distance from the Sun. Only very volatile ices can sublimate there, but volatile retention models such as those by Schaller & Brown (2007) indicate that a body of Huya's size cannot have retained those ices. So the most likely scenario is that Huya does not have an atmosphere of any sort. The ingress and egress data can shed light on an upper limit for a potential atmosphere, but not a very tight one. In any case, we estimate here the upper limit of an atmosphere around Huya, and more precisely, its surface pressure $p_{\rm surf}$. To do so, we have to assume a composition and a temperature profile for this putative atmosphere, which are both unknown.

We may derive some orders of magnitude by assuming that Huya's atmosphere has the same composition (mainly N_2 with traces of CH_4) and same temperature profile as Pluto's atmosphere. This results in a surface temperature of about 36 K, with a rapid increase up to ∼110 K at 30 km altitude due to CH_4 heating, followed by a roughly isothermal upper branch near 100 K.

A ray-tracing scheme (see Dias-Oliveira et al. 2015) then allows us to compare the W-FAST at Wise Observatory data (which is the best data set in terms of temporal sampling and flux dispersion), with models using various values of $p_{\rm surf}$. The results are displayed in Fig. 7. It indicates that an upper limit of about $p_{\rm surf} = 10$ nbar can be placed for a Pluto-like Huya's atmosphere.

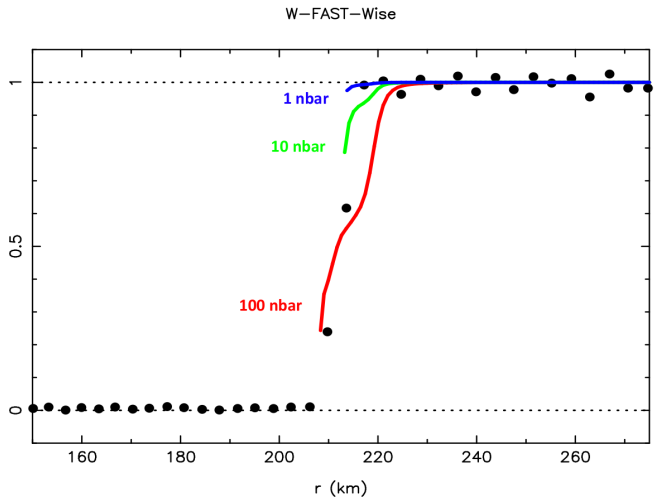

Fig. 7. Comparison of various models assuming a Pluto-like atmosphere (see text for details) with the data obtained at the Wise station with the W-FAST instrument. The data points have been reprojected in the radial direction, merging the ingress and egress part of the light curve. The surface pressures used in each model are indicated next to each curve. The red model ($p_{\rm surf}$ = 100 nbar) can clearly be discarded, considering its discrepancy with the observations. The green model ($p_{\rm surf}$ = 10 nbar) could marginally accommodate the last point just outside the occultation and the rapid drop inside Huya's shadow. The blue model ($p_{\rm surf}$ = 1 nbar) indicates that a 1 nbar atmosphere would go completely unnoticed in the data. We thus estimate that a conservative upper limit of $p_{\rm surf}$ = 10 nbar of a Pluto-like atmosphere is provided by this light curve.

6. Conclusions

This study explores the best ever stellar occultation produced by a TNO in terms of the number of chords, excluding Pluto and the occultation on August 8, 2020 by the TNO 2002 MS_4 (Rommel et al., in prep.). Such a large number of chords, together with a relative small velocity of Huya with respect to the star as seen from Earth (8.07 km s^{-1}), has allowed us to obtain the instantaneous limb of Huya with high precision. Our additional results are as follows:

– An accurate area-equivalent diameter of 411.0 ± 7.3 km was determined from this stellar occultation. This diameter is larger than the radiometric area-equivalent diameter obtained for Huya using *Herschel* and *Spitzer* thermal data when the existence of the satellite is taken into account ($D = 406 \pm 16$ km; Fornasier et al. 2013), but still compatible within error bars.
– After a careful correction of the absolute magnitude of Huya by the rotational phase at the moment of the occultation and by the contribution of the satellite to the total flux of the system, an accurate geometric albedo at *V*-band was obtained: $p_V = 0.079 \pm 0.004$. This albedo is smaller than the radiometric albedo derived from *Herschel* and *Spitzer* measurements ($p_V = 0.083 \pm 0.004$; Fornasier et al. 2013), but we note that the latter is the albedo of the Huya's system, without subtracting the satellite contribution.
– From the occultation results, a 3D shape cannot be confirmed for Huya. The most likely shape is an oblate spheroid (Maclaurin), but a triaxial ellipsoid cannot be totally discarded. In any case, using the occultation results and the information on the rotational light curve (i.e., $P_{\rm preferred} = 6.725$ h and $\Delta m = 0.031$ mag), we can constrain possible 3D solutions for Huya:
  • If Huya's shape is a Maclaurin spheroid, our preferred solution has axes: $2a = 435$ km, $2b = 435$ km, $2c = 233$ km for an aspect angle of 32° and a density of ∼800 kg m^{-3}. The aspect angles for the other possible rotation periods ($P \sim 5.2$ h and $P \sim 4.3$ h) are smaller, however, this case is very unlikely.
  • If Huya's shape is a Jacobi ellipsoid, a family of solutions is possible: $2a$ = [440–455] km, $2b$ = [428–442] km, $2c$ = [253–261] km for aspect angles spanning from 31° to 43° and a minimum density of 859 kg m^{-3}. The minimum densities required for a Jacobi rotating with the other rotational periods are larger and very unlikely for a body of the Huya's size.
– If hydrostatic equilibrium for a homogeneous body is used to explain the occultation results and the rotational light curve, the densities appear to be too high (Jacobi solutions), or the aspect angle is too small (Maclaurin solutions). Alternative 3D shape solutions should invoke non-hydrostatic

equilibrium shapes, which would not require such high densities.
- We did not detect any evidence of the Huya's satellite in any of the light curves (positive or negative) of this occultation.
- No dense rings similar to the structures seen around the dwarf planet Haumea were detected orbiting Huya by means of this occultation, however, very narrow (≤0.1 km) or optically thin rings (opacity ≤ 50%) at different geometries cannot be totally discarded.
- We obtained an upper limit of about $p_{\rm surf} = 10$ nbar for a putative Pluto-like global atmosphere in Huya.

As a general conclusion: From this occultation, we derive the area-equivalent diameter of Huya and the geometric albedo of its surface with high accuracy. We also present and discuss possible 3D shapes based on the occultation data and the rotational light curve. We do not detect any hint of rings around Huya nor any clue of its satellite. Finally, we place constraints on a possible Huya atmosphere using the best-quality occultation light curve.

Acknowledgements. P.S-S. acknowledges financial support by the Spanish grant AYA-RTI2018-098657-J-I00 "LEO-SBNAF" (MCIU/AEI/FEDER, UE). P.S-S., J.L.O., N.M., M.V-L. and R.D. acknowledge financial support from the State Agency for Research of the Spanish MCIU through the "Center of Excellence Severo Ochoa" award for the Instituto de Astrofísica de Andalucía (SEV-2017-0709), they also acknowledge the financial support by the Spanish grants AYA-2017-84637-R and PID2020-112789GB-I00, and the Proyectos de Excelencia de la Junta de Andalucía 2012-FQM1776 and PY20-01309. The research leading to these results has received funding from the European Union's Horizon 2020 Research and Innovation Programme, under Grant Agreement no. 687378, as part of the project "Small Bodies Near and Far" (SBNAF). Part of the research leading to these results has received funding from the European Research Council under the European Community's H2020 (2014–2020/ERC Grant Agreement no. 669416 "LUCKY STAR"). Part of the work of M.P. was financed by a grant of the Romanian National Authority for Scientific Research and Innovation, CNCS – UEFISCDI, PN-III-P1-1.1-TE-2019-1504. This study was financed in part by the Coordenação de Aperfeiçoamento de Pessoal de Nível Superior – Brasil (CAPES) – Finance Code 001 and the National Institute of Science and Technology of the e-Universe project (INCT do e-Universo, CNPq grant 465376/2014-2). The following authors acknowledge the respective CNPq grants: F.B-R 309578/2017-5; R.V.-M. 304544/2017-5, 401903/2016-8; J.I.B.C. 308150/2016-3 and 305917/2019-6; M.A 427700/2018-3, 310683/2017-3 and 473002/2013-2; B.E.M. 150612/2020-6. G.B.R. thanks the support of CAPES and FAPERJ/PAPDRJ (E26/203.173/2016) grant. J.M.O. acknowledges financial support from the Portuguese Foundation for Science and Technology (FCT) and the European Social Fund (ESF) through the PhD grant SFRH/BD/131700/2017. E.F-V. acknowledges funding through the Preeminant Postdoctoral Program of the University of Central Florida. C.K., A.P. and R.S. have been supported by the grants K-125015 and K-138962 of the National Research, Development and Innovation Office (NKFIH, Hungary). E.P. acknowledges the Europlanet 2024 RI project funded by the European Union's Horizon 2020 Research and Innovation Programme (Grant agreement No. 871149). We are grateful to the CAHA and OSN staffs. This research is partially based on observations collected at the Centro Astronómico Hispano Alemán (CAHA) at Calar Alto, operated jointly by Junta de Andalucía and Consejo Superior de Investigaciones Científicas (IAA-CSIC). This research was also partially based on observation carried out at the Observatorio de Sierra Nevada (OSN) operated by Instituto de Astrofísica de Andalucía (CSIC). This article is also based on observations made in the Observatorios de Canarias del IAC with the Liverpool Telescope operated on the island of La Palma by the Instituto de Astrofísica de Canarias in the Observatorio del Roque de los Muchachos. Part of the results were based on observations taken at Pico dos Dias Observatory of the National Laboratory of Astrophysics (LNA/Brazil). Part of the data were collected during the photometric monitoring observations with the robotic and remotely controlled observatory at the University of Athens Observatory – UOAO (Gazeas 2016). We thank the Adiyaman University Astrophysics Application and Research Center for their support in the acquisition of data with the ADYU60 telescope. This work has made use of data from the European Space Agency (ESA) mission *Gaia* (`https://www.cosmos.esa.int/gaia`), processed by the *Gaia* Data Processing and Analysis Consortium (DPAC, `https://www.cosmos.esa.int/web/gaia/dpac/consortium`). Funding for the DPAC has been provided by national institutions, in particular the institutions participating in the *Gaia* Multilateral Agreement.

References

Assafin, M., Vieira Martins, R., Camargo, J. I. B., et al. 2011, in Gaia follow-up network for the solar system objects : Gaia FUN-SSO workshop proceedings, 85
Barucci, M. A., Alvarez-Candal, A., Merlin, F., et al. 2011, Icarus, 214, 297
Benedetti-Rossi, G., Sicardy, B., Buie, M. W., et al. 2016, AJ, 152, 156
Benedetti-Rossi, G., Santos-Sanz, P., Ortiz, J. L., et al. 2019, AJ, 158, 159
Bierson, C. J., & Nimmo, F. 2019, Icarus, 326, 10
Braga-Ribas, F., Sicardy, B., Ortiz, J. L., et al. 2013, ApJ, 773, 26
Braga-Ribas, F., Sicardy, B., Ortiz, J. L., et al. 2014, Nature, 508, 72
Butkevich, A. G., & Lindegren, L. 2014, A&A, 570, A62
Chandrasekhar, S. 1987, Ellipsoidal Figures of Equilibrium, Dover Books on Mathematics (Dover)
de Bergh, C., Boehnhardt, H., Barucci, M. A., et al. 2004, A&A, 416, 791
Desmars, J., Camargo, J. I. B., Braga-Ribas, F., et al. 2015, A&A, 584, A96
Dias-Oliveira, A., Sicardy, B., Lellouch, E., et al. 2015, ApJ, 811, 53
Dias-Oliveira, A., Sicardy, B., Ortiz, J. L., et al. 2017, AJ, 154, 22
Duffard, R., Ortiz, J. L., Thirouin, A., Santos-Sanz, P., & Morales, N. 2009, A&A, 505, 1283
Elliot, J. L., French, R. G., Meech, K. J., & Elias, J. H. 1984, AJ, 89, 1587
Elliot, J. L., Person, M. J., Zuluaga, C. A., et al. 2010, Nature, 465, 897
Fernández-Valenzuela, E., Ortiz, J. L., Duffard, R., Santos-Sanz, P., & Morales, N. 2016, MNRAS, 456, 2354
Fernández-Valenzuela, E., Pinilla-Alonso, N., Stansberry, J., et al. 2021, PSJ, 2, 10
Ferrin, I., Rabinowitz., D., & Schaefer, B., et al. 2001 ApJ, 548, L243
Fornasier, S., Lellouch, E., Müller, T., et al. 2013, A&A, 555, A15
Gaia Collaboration (Prusti, T., et al.) 2016, A&A, 595, A1
Gaia Collaboration (Brown, A. G. A., et al.) 2018, A&A, 616, A1
Gazeas, K. 2016, in Revista Mexicana de Astronomia y Astrofisica Conference Series, 48, 22
Gladman, B., Marsden, B. G., & Vanlaerhoven, C. 2008, Nomenclature in the Outer Solar System, eds. M. A. Barucci, H. Boehnhardt, D. P. Cruikshank, A. Morbidelli, & R. Dotson, 43
Gomes-Júnior, A. R., Morgado, B. E., Benedetti-Rossi, G., et al. 2022, MNRAS, 511, 1167
Grundy, W. M., Porter, S. B., Benecchi, S. D., et al. 2015, Icarus, 257, 130
Grundy, W. M., Noll, K. S., Buie, M. W., et al. 2019, Icarus, 334, 30
Hastings, D. M., Ragozzine, D., Fabrycky, D. C., et al. 2016, AJ, 152, 195
Jewitt, D. C., & Luu, J. X. 2001, AJ, 122, 2099
Licandro, J., Oliva, E., & Di Martino, M. 2001, A&A, 373, L29
Lomb, N. R. 1976, Ap&SS, 39, 447
Merlin, F., Hromakina, T., Perna, D., Hong, M. J., & Alvarez-Candal, A. 2017, A&A, 604, A86
Meza, E., Sicardy, B., Assafin, M., et al. 2019, A&A, 625, A42
Nir, G., Ofek, E. O., Ben-Ami, S., et al. 2021, PASP, 133, 075002
Noll, K. S., Grundy, W. M., Schlichting, H., Murray-Clay, R., & Benecchi, S. D. 2012, IAU Circ., 9253, 2
Ortiz, J. L., Gutiérrez, P. J., Casanova, V., & Sota, A. 2003, A&A, 407, 1149
Ortiz, J. L., Sicardy, B., Braga-Ribas, F., et al. 2012, Nature, 491, 566
Ortiz, J. L., Duffard, R., Pinilla-Alonso, N., et al. 2015, A&A, 576, A18
Ortiz, J. L., Santos-Sanz, P., Sicardy, B., et al. 2017, Nature, 550, 219
Ortiz, J. L., Santos-Sanz, P., Sicardy, B., et al. 2020a, A&A, 639, A134
Ortiz, J. L., Sicardy, B., Camargo, J. I. B., Santos-Sanz, P., & Braga-Ribas, F. 2020b, Stellar occultation by TNOs: from predictions to observations, eds. D. Prialnik, M. A. Barucci, & L. Young, 413
Rommel, F. L., Braga-Ribas, F., Desmars, J., et al. 2020, A&A, 644, A40
Roques, F., Moncuquet, M., & Sicardy, B. 1987, AJ, 93, 1549
Ruprecht, J. D., Bosh, A. S., Person, M. J., et al. 2015, Icarus, 252, 271
Santos-Sanz, P., Ortiz, J. L., Sicardy, B., et al. 2021, MNRAS, 501, 6062
Schaller, E. L., & Brown, M. E. 2007, ApJ, 659, L61
Sheppard, S. S., & Jewitt, D. C. 2002, in ESA Special Publication, Asteroids, Comets, and Meteors: ACM 2002, ed. B. Warmbein, 500, 21
Sicardy, B., Bellucci, A., Gendron, E., et al. 2006, Nature, 439, 52
Sicardy, B., Ortiz, J. L., Assafin, M., et al. 2011, Nature, 478, 493
Sicardy, B., Leiva, R., Renner, S., et al. 2019, Nat. Astron., 3, 146
Sicardy, B., Renner, S., Leiva, R., et al. 2020, The Trans-Neptunian Solar System, eds. Dina Prialnik, Maria Antoinetta Barucci, Leslie Young (Elsevier), 249
Sickafoose, A. A., Bosh, A. S., Levine, S. E., et al. 2019, Icarus, 319, 657
Souami, D., Braga-Ribas, F., Sicardy, B., et al. 2020, A&A, 643, A125
Tancredi, G., & Favre, S. 2008, Icarus, 195, 851
Thirouin, A., Ortiz, J. L., Duffard, R., et al. 2010, A&A, 522, A93
Thirouin, A., Noll, K. S., Ortiz, J. L., & Morales, N. 2014, A&A, 569, A3
van Belle, G. T. 1999, PASP, 111, 1515
Zacharias, N., Monet, D. G., Levine, S. E., et al. 2004, in American Astronomical Society Meeting Abstracts, 205, 48.15

[1] Instituto de Astrofísica de Andalucía (CSIC), Glorieta de la Astronomía s/n, 18008-Granada, Spain,
e-mail: psantos@iaa.es
[2] LESIA, Observatoire de Paris, PSL Research University, CNRS, Sorbonne Université, Univ. Paris Diderot, Sorbonne Paris Cité, France
[3] Astronomical Institute of the Romanian Academy, 5 Cuţitul de Argint, 040557 Bucharest, Romania
[4] Instituto de Astrofísica de Canarias (IAC), C/Vía Láctea s/n, 38205 La Laguna, Tenerife, Spain
[5] Laboratório Interinstitucional de e-Astronomia – LIneA & INCT do e-Universo, Rua Gal. José Cristino 77, Bairro Imperial de São Cristóvão, Rio de Janeiro (RJ), Brazil
[6] UNESP – São Paulo State University, Grupo de Dinâmica Orbital e Planetologia, Guaratinguetá, SP 12516-410, Brazil
[7] Observatório Nacional/MCTI, Rua Gal. José Cristino 77, Bairro Imperial de São Cristóvão, Rio de Janeiro (RJ), Brazil
[8] Universidade Federal do Rio de Janeiro – Observatório do Valongo, Ladeira Pedro Antônio 43, CEP 20.080-090 Rio de Janeiro, RJ, Brazil
[9] Institut Polytechnique des Sciences Avancées IPSA, 63 boulevard de Brandebourg, 94200 Ivry-sur-Seine, France
[10] Institut de Mécanique Céleste et de Calcul des Éphémérides, IMCCE, Observatoire de Paris, PLS Research University, CNRS, Sorbonne Universités, UPMC Univ Paris 06, Univ. Lille, 77 Av. Denfert-Rochereau, 75014 Paris, France
[11] Federal University of Technology – Paraná (UTFPR/Curitiba), Brazil
[12] Florida Space Institute, University of Central Florida, Orlando, FL, USA
[13] ISTEK Belde Observatory, Turkey
[14] Department of Astronomy and Space Sciences, University of Ege, Turkey
[15] Faculty of Physics, University of Bucharest, 405, Atomistilor Street, 077125 Magurele, Ilfov, Romania
[16] Ataturk University, Astrophysics Research & Application Center (ATASAM), 25240 Erzurum, Turkey
[17] Akdeniz University, Faculty of Sciences, Department of Space Sciences and Technologies, 07058 Antalya, Turkey
[18] TÜBITAK National Observatory, Akdeniz University Campus, 07058 Antalya, Turkey
[19] School of Physics and Astronomy and Wise Observatory, Tel Aviv University, Israel
[20] Department of Astronomy and Space Sciences, Science Faculty, Erciyes University, 38030 Melikgazi, Kayseri, Turkey
[21] Particle Physics and Astrophysics Department, Weizmann Institute of Science, Israel
[22] Astronomical Observatory "Amiral Vasile Urseanu" Bucharest, Romania
[23] Space Sciences and Solar Energy Research and Application Center (UZAYMER), Çukurova University, Adana, Turkey
[24] Space Observation and Research Center, Çağ University, Mersin, Turkey
[25] Ege University, Faculty of Science, Department of Physics, 35100 Bornova, Izmir, Turkey
[26] Ataturk University, Science Faculty, Department of Astronomy & Space Sciences, 25240 Erzurum, Turkey
[27] Astronomical Observatory "Victor Anestin" Bacau, Romania
[28] Astroclubul Bucureşti, Romania
[29] Stardust Observatory, Brasov, Romania
[30] St. George Observatory, Ploiești, Romania
[31] Ia cu Stele, Romania
[32] Stardreams Observatory, Valenii de Munte, Romania
[33] ROASTERR-1 Observatory, Cluj-Napoca, Romania
[34] Galaţi Astronomical Observatory, "Răsvan Angheluţă" Museum Complex of Natural Sciences, 6A, Regiment 11 Siret Street, 800340, Galaţi, Romania
[35] Tiraspol State University, 5, Ghenadie Iablocikin Street, 2069 Chișinău, Republic of Moldova
[36] Asociatia Astroclubul Quasar, Romania
[37] Romanian Academy, Cluj-Napoca Branch, Astronomical Observatory Cluj-Napoca, Str. Cireşilor, Nr. 19, 400487, Cluj-Napoca, Romania
[38] Barlad Observatory, Romania
[39] Institute of Astronomy, V.N. Karazin Kharkiv National University, Ukraine
[40] QOS Observatory, National Space Facilities Control and Test Center, Ukraine
[41] Section of Astrophysics, Astronomy and Mechanics, Department of Physics, National and Kapodistrian University of Athens, 15784 Zografos, Athens, Greece
[42] Astronomical Observatory of Odessa I.I. Mechnikov National University, Shevchenko Park, Odessa 65014, Ukraine
[43] Konkoly Observatory, Research Centre for Astronomy and Earth Sciences, Eötvös Loránd Research Network (ELKH), 1121 Budapest, Konkoly Thege Miklós út 15–17, Hungary
[44] ELTE Eötvös Loránd University, Institute of Physics, Budapest, Hungary
[45] Çanakkale Onsekiz Mart University, Faculty of Arts and Sciences, Department of Physics, 17020, Çanakkale, Turkey
[46] Çanakkale Onsekiz Mart University, Astrophysics Research Center and Ulupınar Observatory, 17020, Çanakkale, Turkey
[47] Northolt Branch Observatories, UK
[48] Sainte Marie, La Réunion, France
[49] Agrupació Astronòmica de Sabadell, Barcelona, Spain
[50] International Occultation Timing Association–European Section (IOTA-ES), Germany
[51] Almalex Observatory, Leeds, UK
[52] Les Makes, La Réunion, France
[53] Ellinogermaniki Agogi Observatory, Athens, Greece
[54] Ondokuz Mayis University Observatory, Space Research Center, 55200, Kurupelit, Samsun, Turkey
[55] Laboratory of Space Researches, Uzhhorod National University, Uzhhorod, Daleka Str., 2A, Uzhhorod 88000, Ukraine
[56] Astronomical Observatory Institute, Faculty of Physics, A. Mickiewicz University, Słoneczna 36, 60-286 Poznań, Poland
[57] Mt. Suhora Observatory, Pedagogical University, ul. Podchorazych 2, PL-30-084 Krakow, Poland
[58] Department of Physics, Faculty of Science and Arts, İnönü University, Malatya, Turkey
[59] Astronomical Observatory, Institute of Theoretical Physics and Astronomy, Vilnius University, Sauletekio av. 3, 10257 Vilnius, Lithuania
[60] Janusz Gil Institute of Astronomy, University of Zielona Góra, Prof. Szafrana 2, PL-65-516 Zielona Góra, Poland

Appendix A: Additional tables

Table A.1. Observation details of the stellar occultation by the TNO Huya.

Chord number	Observatory (Country) IAU code	Latitude (N) Longitude (E) Altitude (m)	Telescope diameter (m) Detector	Exposure time Cycle time (seconds)	Observer(s)	Detection $\sigma_{\rm flux}$
1	TÜBITAK National Observatory-1 (Turkey) A84	36° 49' 17.1" 30° 20' 08.0" 2470	1.0 SI 1100 Cryo	2.0 7.44	Y. Kilic, T. Ozisik O. Erece, S.E. Kilic	Positive 0.021
2	TÜBITAK National Observatory-2 (Turkey) A84	36° 49' 29.1" 30° 20' 08.2" 2455	0.60 FLI Proline 3041	15.0 20.0	Y. Kilic, T. Ozisik O. Erece, S.E. Kilic	Positive 0.048
3	Romanian Academy, Astron. Obs. Cluj, Feleacu Station (Romania) —	46° 42' 37.6" 23° 35' 35.7" 783	0.30 SBIG STT-1603ME	4.0 4.5	V. Turcu	Positive 0.038
4	ROASTERR-1 Observatory (Romania) L04	46° 49' 15.6" 23° 35' 47.0" 390	0.30 ASI 120MM	0.2 0.5	L. Hudin	Positive 0.093
5	W-FAST at Wise Observatory (Israel) 097	30° 35' 48.0" 34° 45' 48.0" 900	0.57 Andor Zyla	1.0 1.007	G. Nir	Positive 0.015
6	C18 at Wise Observatory (Israel) 097	30° 35' 48.0" 34° 45' 48.0" 900	0.45 QSI 683	3.0 4.46	S. Kaspi	Positive 0.009
7	Astronomical Inst. of Romanian Academy-1 (Romania) 073	44° 24' 43.2" 26° 05' 38.2" 83	0.50 FLI PL16803	2.0 4.2	A. Sonka S. Anghel	Positive 0.047
8	Astronomical Inst. of Romanian Academy-2 (Romania) 073	44° 24' 48.0" 26° 05' 48.0" 81	0.50 Andor Zyla	1.0 1.025	D.A. Nedelcu	Positive 0.041
9	ISTEK Belde Observatory (Turkey) —	41° 01' 49.3" 29° 02' 33.6" 150	0.40 Sony IMX236LQJ CMOS	0.8 0.8	M. Acar A. Ateş C. Kayhan	Positive 0.088
10	Amateur Observatory-1 (Romania) —	44° 55' 05.0" 25° 58' 12.1" 167	0.15 QHY6 CCD	4.0 6.0	E. Petrescu	Positive 0.030
11	St. George Observatory (Romania) L15	45° 00' 25.2" 25° 58' 42.2" 242	0.18 ATIK 460EX	3.0 4.0	C. Danescu	Positive 0.026
12	Amateur Observatory-2 (Romania) —	44° 26' 36.5" 26° 31' 12.5" 65	0.20 ASI 1600MM	0.20 0.25	V. Dumitrescu	Positive 0.053
13	Stardust Observatory (Romania) L13	45° 38' 30.0" 25° 37' 19.0" 597	0.20 CCD Atik 383L+mono (KAF8300)	8.0 12.0	L. Curelaru	Positive 0.016
14	Stardreams Observatory (Romania) L16	45° 12' 13.3" 26° 02' 44.2" 379	0.20 ZWO ASI120MM-S	1.0 1.01	R. Gherase	Positive 0.074
15	Martin S. Kraar Obs. / Weizmann Inst. (Israel) C78	31° 54' 29.0" 34° 48' 45.0" 107	0.40 QHY 367C	1.0 3.83	I. Manulis	Positive 0.056
⋆	Amateur Observatory-3 (Romania) —	47° 05' 02.3" 24° 23' 30.9" 331	0.40 Watec 902H2 Ultimate	0.0333 0.0333	R. Truta	Positive 0.074
16	Amateur Observatory-4 (Romania) —	44° 45' 41.5" 27° 20' 25.1" 41	0.20 QHY 163M-CMOS	0.20 0.25	D. Berteşteanu	Positive 0.093
17	Bacau Observatory (Romania) L57	46° 33' 56.3" 26° 54' 15.0" 170	0.35 SBIG STL 6303E	2.0 9.0	R. Anghel	Positive 0.026
18	Galati Observatory-1 (Romania) C73	45° 25' 07.9" 28° 01' 57.0" 31	0.40 CCD SBIG STL-6303E	20.0 24.8	J.O. Tercu A.-M. Stoian	Positive 0.011
18	Galati Observatory-2 (Romania) C73	45° 25' 07.9" 28° 01' 57.0" 31	0.20 CCD Atik 383L+Mono	20.0 31.3	J.O. Tercu A.-M. Stoian	Positive 0.031
19	Barlad Observatory (Romania) L22	46° 13' 54.1" 27° 40' 10.2" 70	0.20 ASI 1600	0.50 0.82	C. Vantdevara	Positive 0.068
	QOS Observatory (Ukraine) L18	48° 50' 54.0" 26° 43' 12.0" 352	0.30 ZWO ASI 174MM	0.2 0.200016	T. O. Dementiev O. M. Kozhukhov	Negative 0.106
	Çukurova University (Turkey) —	37° 03' 23.0" 35° 21' 04.0" 130	0.50 Orion Parsec 8300M	90 108	A. Solmaz M. Tekes	Negative 0.027

This Table includes the sites from where the occultation was detected and the closest negatives used to constrain the instantaneous shape of the object. $\sigma_{\rm flux}$ is the flux dispersion, i.e. the standard deviation of the normalized flux (outside of the occultation in the case of positive detections). Sites are sorted by their distance to the center of the predicted shadow path, from West to East. The data from the site marked with ⋆ was not used in the final analysis of the occultation (see Section 3 for a detailed explanation).

Table A.2. Summary table of the observing campaign.

Observatory (Country) IAU code	Latitude (N) Longitude (E) Altitude (m)	Telescope aperture (m)	Observer(s)	Observation
Sant Esteve Sesrovires (Spain) –	41° 29’ 37.5” 01° 52’ 21.1” 180	0.40	C. Schnabel	Negative
Sabadell Observatory (Spain) 619	41° 33’ 00.2” 02° 05’ 24.6” 224	0.50	C. Perello A. Selva	Negative
Normandy (France) –	49° 36’ 26.4” 358° 46’ 03.3” 12	0.14	J. Lecacheux	Negative
Northolt Branch Observatories (UK) Z80	51° 33’ 16.8" 359° 37’ 41.1" 55	0.25	G. Wells D. Bamberger	Negative
Almalex Observatory (UK) Z92	53° 50’ 15.4" 358° 23’ 32.0" 114	0.28	A. Pratt	Negative
NOAK Observatory (Greece) L02	39° 39’ 08.8” 20° 48’ 59.7” 546	0.25	N. Sioulas	Bad weather
Univ. of Athens Observatory - UOAO (Greece) –	37° 58’ 06.8” 23° 47’ 00.1” 250	0.40	K. Gazeas E. Karampotsiou	Negative
Ellinogermaniki Agogi Observatory (Greece) C68	37° 59’ 52.3” 23° 53’ 36.1” 162	0.40	V. Tsamis K. Tigani	Negative
Konkoly Observatory Budapest (Hungary) 053	47° 29’ 59.3” 18° 57’ 51.1” 469	0.60	A. Pal R. Szakats	Bad weather
Ulupınar Observatory (Turkey) –	40° 06’ 01.0” 26° 28’ 32.0” 410	0.40	C. Puskullu	Negative
Berlin (Germany) –	52° 30’ 58.0" 13° 25’ 40.0" 37	0.20	C. Weber	Negative
Konkoly Observatory Piszkestető (Hungary) 561	47° 55’ 06.0” 19° 53’ 41.7” 944	1.00	A. Pal R. Szakats	Negative
TÜBITAK National Observatory-1 (Turkey) A84	36° 49’ 17.1" 30° 20’ 08.0" 2472	1.00	Y. Kilic, T. Ozisik O. Erece, S.E. Kilic	Positive
TÜBITAK National Observatory-2 (Turkey) A84	36° 49’ 29.1" 30° 20’ 08.2" 2472	0.60	Y. Kilic, T. Ozisik O. Erece, S.E. Kilic	Positive
Akdeniz University Observatory (Turkey) –	36° 49’ 27.0” 30° 20’ 08.0” 2490	0.25	V. Bakış H. Bakış Z. Eker	Technical problems
Mt. Suhora Observatory (Poland) –	49° 34’ 09.0” 20° 04’ 03.0” 1009	0.60	W. Ogłoza	Bad weather
Borowiec Observatory (Poland) 187	52° 16’ 37.2” 17° 04’ 28.6” 123	0.40	A. Marciniak	Bad weather
Romanian Acad., Astron. Obs. Cluj, Feleacu Station (Romania) –	46° 42’ 37.6” 23° 35’ 35.7” 783	0.30	V. Turcu	Positive
ROASTERR-1 Observatory (Romania) L04	46° 49’ 15.6” 23° 35’ 47.0” 390	0.30	L. Hudin	Positive

continued on next page

Table A.2 - Summary table of the observing campaign *(continued from previous page)*

Observatory (Country) IAU code	Latitude (N) Longitude (E) Altitude (m)	Telescope aperture (m)	Observer(s)	Observation
W-FAST at Wise Observatory (Israel) 097	30° 35' 48.0" 34° 45' 48.0" 900	0.57	G. Nir	Positive
C18 at Wise Observatory (Israel) 097	30° 35' 48.0" 34° 45' 48.0" 900	0.45	S. Kaspi	Positive
Astronomical Inst. of Romanian Academy-1 (Romania) 073	44° 24' 43.2" 26° 05' 38.2" 83	0.50	A. Sonka S. Anghel	Positive
Astronomical Inst. of Romanian Academy-2 (Romania) 073	44° 24' 48.0" 26° 05' 48.0" 81	0.50	D.A. Nedelcu	Positive
Astroclubul Bucureşti (Romania) –	44° 24' 49.0" 26° 05' 48.1" 69	0.40	Z. Deak	Technical problems
ISTEK Belde Observatory (Turkey) –	41° 01' 49.3" 29° 02' 33.6" 150	0.40	M. Acar A. Ateş C. Kayhan	Positive
ISTEK Belde Observatory (Turkey) –	41° 01' 49.3" 29° 02' 33.6" 150	0.35	M. Acar A. Ateş C. Kayhan	Technical problems
ISON-Uzhgorod Observatory "Derenivka" (Ukraine) K99	48° 33' 48.2" 22° 27' 12.6" 213	0.40	V. Kudak V. Perig	Bad weather
Amateur Observatory-1 (Romania) –	44° 55' 05.0" 25° 58' 12.1" 167	0.15	E. Petrescu	Positive
St. George Observatory (Romania) L15	45° 00' 25.2" 25° 58' 42.2" 242	0.18	C. Danescu	Positive
Amateur Observatory-2 (Romania) –	44° 26' 36.5" 26° 31' 12.5" 65	0.20	V. Dumitrescu	Positive
Stardust Observatory (Romania) L13	45° 38' 30.0" 25° 37' 19.0" 597	0.20	L. Curelaru	Positive
Stardreams Observatory (Romania) L16	45° 12' 13.3" 26° 02' 44.2" 379	0.20	R. Gherase	Positive
Martin S. Kraar Obs./ Weizmann Inst. (Israel) C78	31° 54' 29.0" 34° 48' 45.0" 107	0.40	I. Manulis	Positive
Amateur Observatory-3 (Romania) –	47° 05' 02.3" 24° 23' 30.9" 331	0.40	R. Truta	Positive
Amateur Observatory-4 (Romania) –	44° 45' 41.5" 27° 20' 25.1" 41	0.20	D. Berteşteanu	Positive
Bacau Observatory (Romania) L57	46° 33' 56.3" 26° 54' 15.0" 170	0.35	R. Anghel	Positive
Galați Observatory-1 (Romania) C73	45° 25' 07.9" 28° 01' 57.0" 31	0.40	J.O. Tercu A.-M. Stoian	Positive
Galați Observatory-2 (Romania) C73	45° 25' 07.9" 28° 01' 57.0" 31	0.20	J.O. Tercu A.-M. Stoian	Positive
Barlad Observatory	46° 13' 54.1"	0.20		Positive

continued on next page

Table A.2 - Summary table of the observing campaign *(continued from previous page)*

Observatory (Country) IAU code	**Latitude (N) Longitude (E) Altitude (m)**	**Telescope aperture (m)**	**Observer(s)**	**Observation**
(Romania) L22	27° 40’ 10.2” 70		C. Vantdevara	
QOS Observatory (Ukraine) L18	48° 50’ 54.0” 26° 43’ 12.0” 352	0.30	T. O. Dementiev O. M. Kozhukhov	Negative
Çukurova University (Turkey) –	37° 03’ 23.0” 35° 21’ 04.0” 130	0.50	A. Solmaz M. Tekes	Negative
Odessa Astronomical Observatory, Mayaky (Ukraine) 583	46° 23’ 49.1” 30° 16’ 16.6” 18	0.80	V. Kashuba V. Zhukov	Negative
Adiyaman (Turkey) –	38° 13’ 31.2” 37° 45’ 06.1” 690	0.60	M. Żejmo	Bad weather
Ondokuz Mayıs University (Turkey) –	41° 22’ 04.0” 36° 12’ 06.0” 151	0.35	S. Kalkan	Technical problems
Moletai (Lithuania) –	55° 18’ 57.5" 25° 33’ 48.0" 200	0.35	E. Pakštienė	Bad weather
İnönü University Observatory (Turkey) –	38° 19’ 24.0” 38° 26’ 13.0” 130	0.35	T. Ozdemir	Bad weather
Makes Observatory-La Reunion (France) –	-21° 11’ 56.1” 55° 24’ 36.3” 997	0.18	J.P. Teng	Negative
Sainte Marie-La Reunion (France) –	-20° 53’ 48.5" 55° 34’ 00.1" 54	0.20	B. Mondon	Negative
Ataturk University (Turkey) –	39° 54’ 17.1” 41° 14’ 40.1” 1857	0.50	C. Yesilyaprak O. Satir, M.S. Niaei E. Atalay	Negative

This table includes all the telescopes and observers that supported the Huya occultation campaign. Sites are sorted by their distance to the center of the predicted shadow path, from west to east.

Table A.3. Ingress and egress times derived from the Huya occultation light curves.

#chord	Observatory, Country	Ingress (UT)	Egress (UT)	Chord size (km)
1	TÜBITAK National Observatory-1, Turkey	00:52:34.387±2.592	00:53:00.703±0.142	212.4±22.1
2	TÜBITAK National Observatory-2, Turkey	00:52:30.407±5.500	00:52:52.439±5.500	177.8±88.8
3	Romanian Acad., Astron. Obs. Cluj, Feleacu Sta., Romania	00:53:51.515±0.115	00:54:37.293±0.089	369.4±1.7
4	ROASTERR-1 Observatory, Romania	No data	00:54:38.748±0.030	—
5	W-FAST-Wise Observatory, Israel	00:51:21.416±0.016	00:52:07.918±0.023	375.3±0.3
6	C18 at Wise Observatory, Israel	00:51:21.110±0.040	00:52:07.851±0.040	377.2±0.7
7	Astronomical Inst. Romanian Academy-1, Romania	00:53:30.014±0.998	00:54:18.863±0.098	394.2±8.8
8	Astronomical Inst. Romanian Academy-2, Romania	00:53:31.111±0.041	00:54:18.814±0.041	385.0±0.7
9	ISTEK Belde Observatory, Turkey	00:52:59.908±0.062	00:53:50.451±0.083	407.9±1.2
10	Amateur Observatory-1, Romania	00:53:33.562±0.444	00:54:23.630±0.174	404.1±5.0
11	St. George Observatory, Romania	00:53:34.446±0.083	00:54:24.868±0.077	406.9±1.3
12	Amateur Observatory-2, Romania	00:53:30.484±0.020	00:54:21.217±0.200	409.4±1.8
13	Stardust Observatory, Romania	00:53:38.100±0.150	00:54:29.800±1.850	417.2±16.1
14	Stardreams Observatory, Romania	00:53:37.111±0.098	00:54:29.122±0.099	419.7±1.6
15	Martin S. Kraar Obs., Israel	00:51:30.046±0.100	00:52:23.578±1.148	432.0±10.1
⋆	Amateur Observatory-3, Romania	00:00:00.000±0.007	00:00:43.218±0.007	348.8±0.1
16	Amateur Observatory-4, Romania	00:53:33.840±0.027	00:54:25.060±0.027	413.4±0.4
17	Bacau Observatory, Romania	00:53:46.520±3.400	00:54:33.919±0.083	382.5±28.1
18	Galați Observatory-1 and 2, Romania	00:53:40.500±0.440	00:54:25.420±0.440	362.5±7.1
19	Barlad Observatory, Romania	00:53:51.192±0.047	00:54:31.753±0.073	327.3±1.0

Sites are sorted by their distance to the center of the predicted shadow path, from west to east. The chord marked with ⋆ was not used in the final analysis of the occultation (see Section 3).

Table A.4. Parameters of the best-fitting ellipse.

$(a'$, $b')$	(217.6 ± 3.5 km , 194.1 ± 6.1 km)
$(f_c$, $g_c)$	(2984.7 ± 3.2 km , -1850.9 ± 1.7 km)
P′	55.2°± 9.1
D_{eq}	411.0 ± 7.3 km
p_V	0.079 ± 0.004

Parameters of the best-fitting ellipse obtained from the occultation chords plus the closest non-detection constraint (Figure 6). The area-equivalent diameter (D_{eq}) and geometric albedo (p_V) derived from this limb fit are also included (see Section 5.1 for details).

Table A.5. Ring constraints not accounting for dead-times.

Observatory (Telesc., Country)	**w (km)**	**op$_{min}$**	**w(op=50%) (km)**	**w(op=100%) (km)**
TÜBITAK National Observatory-1 (1.00 m, Turkey)	16.1	6.3%	2.0	1.0
TÜBITAK National Observatory-2 (0.60 m, Turkey)	121.1	14.4%	34.9	17.4
Romanian Academy, Astronomical Observatory Cluj, Feleacu Station (0.30 m, Romania)	32.3	11.4%	7.4	3.7
ROASTERR-1 Observatory (0.30 m, Romania)	1.6	27.9%	0.9	0.5
W-FAST at Wise Observatory (0.57 m, Israel)	8.1	4.5%	0.7	0.4
C18 at Wise Observatory (0.45 m, Israel)	24.2	2.7%	1.3	0.7
Astronomical Inst. of Romanian Academy-1 (0.50 m, Romania)	16.1	14.1%	4.6	2.3
Astronomical Inst. of Romanian Academy-2 (0.50 m, Romania)	8.1	12.3%	2.0	1.0
ISTEK Belde Observatory (0.40 m, Turkey)	6.5	26.4%	3.4	1.7
Amateur Observatory-1 (0.15 m, Romania)	32.3	9.0%	5.8	2.9
St. George Observatory (0.18 m, Romania)	24.2	7.8%	3.8	1.9
Amateur Observatory-2 (0.20 m, Romania)	1.6	15.9%	0.5	0.3
Stardust Observatory (0.20 m, Romania)	64.6	4.8%	6.2	3.1
Stardreams Observatory (0.20 m, Romania)	8.1	22.2%	3.6	1.8
Martin S. Kraar Obs./Weizmann Inst. (0.40 m, Israel)	8.1	16.8%	2.7	1.4
Amateur Observatory-3 (0.40 m, Romania)	0.3	22.2%	0.1	0.1
Amateur Observatory-4 (0.20 m, Romania)	1.6	27.9%	0.9	0.5
Bacau Observatory (0.35 m, Romania)	16.1	7.8%	2.5	1.3
Galați Observatory-1 (0.40 m, Romania)	161.4	3.3%	10.7	5.3
Galați Observatory-2 (0.20 m, Romania)	161.4	9.3%	30.0	15.0
Barlad Observatory (0.20 m, Romania)	4.0	20.4%	1.6	0.8
QOS Observatory (NEGATIVE) (0.30 m, Ukraine)	1.6	31.8%	1.0	0.5

Ring width (w) and minimum opacity (op$_{min}$) for a 3σ detection, obtained from all the telescopes that detected the occultation and the closest negative one. In the third and fourth column we estimate the ring width detectable at 3σ level for opacities of 50% and 100% (completely opaque ring), respectively.